Nanoscale

ROYAL SOCIETY OF CHEMISTRY

PAPER

View Article Online
View Journal | View Issue

Cite this: *Nanoscale*, 2020, **12**, 22245

Self-assembly of amphiphilic polyoxometalates for the preparation of mesoporous polyoxometalate-titania catalysts†

Andi Di,[a] Julien Schmitt,[a,b] Marcelo Alves da Silva,[a] Kazi M. Zakir Hossain,[a] Najet Mahmoudi,[c] R. John Errington[d] and Karen J. Edler *[a]

Received 14th August 2020,
Accepted 22nd October 2020

DOI: 10.1039/d0nr05967f

rsc.li/nanoscale

Amphiphilic polyoxometalate (POM) surfactants were prepared by covalently grafting double hydrophobic tails with chain lengths $C_{12}H_{25}$, $C_{14}H_{29}$, $C_{16}H_{33}$ or $C_{18}H_{37}$ onto the lacunary Wells–Dawson $\{P_2W_{17}O_{61}\}$ headgroup. The critical micelle concentrations (CMCs) of these novel surfactants in aqueous solutions were determined by conductivity, and micelle formation was studied by small angle neutron scattering (SANS). Surprisingly, the amphiphiles with longer hydrophobic tails tend to form less elongated and more globular micelles in water. The self-assembled amphiphilic polyoxometalates were used as templates in the hydrothermal synthesis of mesoporous TiO_2 containing dispersed, immobilised $\{P_2W_{17}O_{61}\}$ units, which showed enhanced activity for the photodegradation of rhodamine B (RhB). The catalyst was recycled eight times with no loss of efficiency, demonstrating the stability of the hybrid structure. The amphiphilic polyoxometalates, therefore have excellent potential for the synthesis of various types of catalytically active porous materials.

Introduction

Polyoxometalates (POMs) are a class of unique nanoscale transition metal oxide clusters, formed by earth-abundant metals in their highest oxidation states.[1,2] Due to their remarkable redox and photochemical properties, they are often used as catalysts for selective reduction[3,4] and as inexpensive photocatalysts for the green removal of organic pollutants or transition metals from water.[5,6] Similar to semiconductor photocatalysts, which experience electron transfer from the valence band (VB) to the conduction band (CB) under ultraviolet irradiation, POMs undergo electron transfer from the oxygen-based highest occupied molecular orbitals (HOMO) to the lowest unoccupied molecular orbitals (LUMO) on the addenda atoms under UV irradiation,[7,8] resulting in a colour change to blue. The charge-transfer excited state POM (POM*) has a highly oxidizing power that is strong enough to oxidise organic species or to generate $^{\bullet}OH$ radicals.[9,10]

The incorporation of POMs onto conventional supports, such as SiO_2,[11,12] TiO_2,[13,14] Al_2O_3 [11] or metal–organic frameworks,[15] through direct dispersion has been investigated to increase the application of POMs for catalysis. However, it has been reported that POMs anchored onto the surface of such supports are not stable since the POMs may be leached out by water or alcohol.[16] Studies have therefore been undertaken to modify the inner walls of the support materials to improve POM adhesion: *e.g.* by grafting organic moieties such as aminosilane or imidazole, to provide strong anchoring of POMs and prevent POM leaching when applied as a catalyst in polar solvent media.[16–19] However, this method limits the applications of these materials due to the low thermal stability of the organic anchoring groups at high temperatures.[20] Alternatively, researchers have been exploring the encapsulation of POMs into aggregates formed by surfactants or polymers,[21–23] with the aim to fabricate polyoxometalate-decorated mesoporous materials *via* a one-pot synthesis.

Amphiphilic surfactants are of great interest for their applications as templates in the formation of mesoporous materials, which typically form from mixed aqueous solutions of surfactants and inorganic precursors.[24–26] Porosity is generated in the inorganic materials after the removal of the organic components from the surfactant template. These mesoporous materials, due to their high specific surface areas and uniform

[a]*Department of Chemistry, University of Bath, Claverton Down, Bath, BA2 7AY, UK. E-mail: k.edler@bath.ac.uk*
[b]*LSFC Laboratoire de Synthèse et Fonctionnalisation des Céramiques, UMR 3080 CNRS/Saint-Gobain CREE, Saint-Gobain Research Provence, 550 avenue Alphonse Jauffret, Cavaillon, France*
[c]*ISIS Neutron and Muon Source, Science and Technology Facilities Council, Rutherford Appleton Laboratory, Didcot OX11 0QX, UK*
[d]*Chemistry, School of Natural and Environmental Sciences, Newcastle University, Newcastle upon Tyne, NE1 7RU, UK*

†Electronic supplementary information (ESI) available. See DOI: 10.1039/D0NR05967F

mesopore size, are particularly interesting as supports for catalysts.[27,28]

To incorporate POMs into the matrix of inorganic mesostructured materials or synthesise porous hybrid materials where the POMs are accessible, a POM-based amphiphile that can be used as a templating agent is key. Self-assembly is an efficient method to synthesise materials with high surface areas and open networks, and hence the use of POM amphiphiles has the potential to organise accessible polyoxometalates directly and uniformly within the supports. There have been previous reports on the synthesis of surfactants with POMs as headgroups through covalent bonding,[29–33] but to the best of our knowledge, there have been no detailed studies of the application of POM-based amphiphiles to template mesoporous POM-decorated inorganic materials.

Among various oxide semiconductor photocatalyst materials, titania is recognised as the most suitable material for widespread environmental applications due to its low cost, strong oxidizing ability and photostability.[34,35] Its performance is often reinforced through the incorporation of electron-transporting materials, such as graphene oxide[36] or graphene,[37] within the titania matrix. Also, there have been attempts to load polyoxometalates onto TiO_2 through a layer by layer strategy, physical mixing or electrostatic bonding.[38–40] These studies have demonstrated synergistic effects between TiO_2 and polyoxometalates.

In this paper, we report the characterisation of micellar structures formed by amphiphilic $[P_2W_{17}O_{61}\{OSi_2(C_nH_{2n+1})_2\}]^{6-}$ (Wells–Dawson type POMs with double hydrocarbon tails C_nH_{2n+1}, denoted as POM-2C$_n$, with molecular structure illustrated in Fig. 1), the influence of the tail length of the amphiphiles on the micelle shape and degree of counterion ionisation, using conductivity, small angle neutron scattering (SANS), zeta-potential and dynamic light scattering (DLS).

The Wells–Dawson anion $[\alpha\text{-}P_2W_{18}O_{62}]^{6-}$ can readily accept multiple electrons without any change in the cluster geometry, and both $[\alpha\text{-}P_2W_{18}O_{62}]^{6-}$ and its lacunary derivative $[P_2W_{17}O_{61}]^{10-}$ are often used as co-catalysts for catalytic oxidation and photocatalytic reduction.[41,42] The siloxane derivatives $[P_2W_{17}O_{61}\{OSi_2(C_nH_{2n+1})_2\}]^{6-}$ are amphiphiles with redox-active metal oxide headgroups and form micelles in water. Therefore, these micelles were used directly as templating agents for the hydrothermal synthesis of POM-TiO_2 mesoporous materials, without the addition of any other co-templating agents. The resulting POM-TiO_2 hybrid materials have relatively high surface areas and better rhodamine B (RhB) photodegradation properties compared to a porous TiO_2 material prepared using a commercial anionic surfactant template.

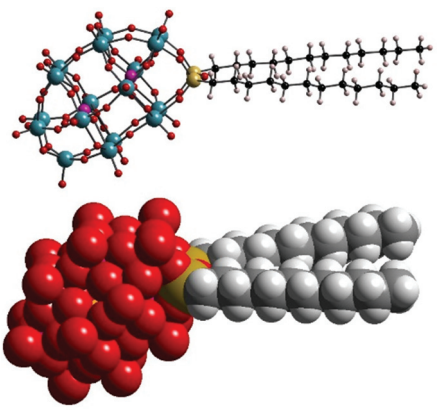

Fig. 1 Ball-and-stick and space-filling representations of the structure of the $[P_2W_{17}O_{61}\{OSi_2(C_nH_{2n+1})_2\}]$ anion (R = $C_{12}H_{25}$) POM-2C$_{12}$. Colour code: W (blue), P (purple), O (red), Si (yellow), C (black) and H (white).

Experimental

Materials

$Na_2WO_4{\cdot}2H_2O$ (purity >99%), phosphoric acid (85 wt% in water solution), NH_4Cl (purity >99.5%), KCl (laboratory reagent grade), dodecyltrichlorosilane ($C_{12}H_{25}SiCl_3$, purity >95%), octadecyltrichlorosilane ($C_{18}H_{37}SiCl_3$, purity >90%), $KHCO_3$ (purity >99.7%), sodium dodecyl sulfate (SDS, purity >99%) and D_2O (99.9 atom% D) were purchased from Sigma Aldrich. Tetradecyltrichlorosilane ($C_{14}H_{29}SiCl_3$, purity 98%) and hexadecyltrichlorosilane ($C_{16}H_{33}SiCl_3$, purity 98%) were purchased from Fluorochem. All chemicals were used without further purification. 70 mol% D_2O in H_2O was prepared using ultrapure water (18.2 MΩ cm, from an ELGA PURELAB flex water purification system).

Preparation of POM-2C$_n$

$K_6[\alpha\text{-}P_2W_{18}O_{62}]{\cdot}14H_2O$ was prepared as previously described by Droege.[43] Lacunary $K_{10}[\alpha\text{-}P_2W_{17}O_{61}]{\cdot}19H_2O$ was synthesised according to the method of Finke *et al.*,[44] and then used to prepare POM-2C$_n$. A typical reaction is as follows: $K_{10}[\alpha\text{-}P_2W_{17}O_{61}]{\cdot}19H_2O$ (1.040 mmol) was dispersed in anhydrous MeCN (180 ml) and stirred under nitrogen for 4 hours. Trichlorosilane, $RSiCl_3$ (R = $C_{12}H_{25}$, $C_{14}H_{29}$, $C_{16}H_{33}$ or $C_{18}H_{37}$, 4.94 mmol) was dissolved in anhydrous dichloromethane (60 ml), then added dropwise to POM suspension with stirring. The obtained mixture was stirred for 12 hours to finish the reaction.

The mixture produced was filtered and then dried using a rotary-evaporator. The powder obtained was washed four times with anhydrous diethyl ether (50 ml) to remove the excess of trichlorosilane, and was vacuum-dried to give the final product $K_6[P_2W_{17}O_{61}\{OSi_2(C_nH_{2n+1})_2\}]$, denoted as POM-2C$_n$, with n = 12, 14, 16 or 18.

Synthesis of POM-TiO_2

The nPOM-TiO_2 hybrid materials were prepared by mixing an aqueous HCl solution (pH = 2) of POM-2C$_n$ (9.17 mM, 9 ml) and an aqueous HCl solution (pH = 2) of $TiOSO_4$ (0.672 M, 6 ml) to give final POM-2C$_n$ and $TiOSO_4$ concentrations of 5.5 mM and 0.269 M respectively. The reaction was performed at 150 °C in an autoclave with a ramping rate of 5 °C min^{-1}, and then was held at 150 °C for 20 hours. The obtained powder was filtered and washed with water to remove any surfactant excess prior to freeze-drying. The freeze-dried powder

was calcined at 500 °C in air for 5 hours to remove the hydrocarbon tails to generate pores. The effect of temperature on Dawson structured POMs has been extensively studied previously in the literature.[45–47] According to these studies, the Wells–Dawson conformation of the POM is maintained up to 873 K, which is well above the calcination temperature of our materials. The calcined products were porous TiO_2 materials containing functionalised POM units, and were labelled *n*POM-TiO_2 catalyst with n = 12, 16 or 18 depending on the tail length of the POM-2C$_n$ used in the synthesis. For comparison, a sample of TiO_2 templated by sodium dodecyl sulfate (SDS) was synthesised according to the procedure already described in the literature which used a much higher surfactant concentration (0.26 M SDS) than that used for POM-2C$_n$ templating.[48] To study the effect of POM-2C$_n$ surfactant concentration on the material formed, a second 16POM-TiO_2 hybrid material was prepared at a higher concentration of POM-2C$_{16}$ (22.0 mM) using the same method described above; the resulting material is labelled as 16POM-TiO_2-2.

The synthesised materials were characterised using transmission electron microscopy (TEM), nitrogen sorption, powder X-ray diffraction (PXRD) and energy dispersive X-ray (EDX) elemental mapping.

Photocatalytic activity test

0.015 g *n*POM-TiO_2 or SDS templated TiO_2 catalyst was added to 30 ml of an aqueous mixture of RhB (15 mg L^{-1}; 0.031 mM) and H_2O_2 (1.5 mM). The mixture was exposed to solar light (energy equal to one sun) under stirring for 80 min. During this time 2 mL aliquots of solution were removed from the system every 20 min and centrifuged. UV-vis absorption measurements were conducted on the clear solutions obtained to determine the concentration of rhodamine B (RhB) according to the major absorption intensity at 553 nm, for each degradation stage. The measured solution was added back to the system at every stage to maintain the total volume. A blank experiment was carried out as follows: a 30 ml of an aqueous mixture of RhB (15 mg L^{-1}; 0.031 mM) and H_2O_2 (1.5 mM) was illuminated by solar light without adding any photocatalyst. The change of RhB concentration with illumination time was recorded using the same method as above.

A control experiment was performed by using 0.20 mg POM-2C$_{12}$ (4×10^{-5} mmol, equivalent to the moles of POM in 0.015 grams of 12POM-TiO_2 material estimated by using the EDX elemental mapping result) as the catalyst. A bathochromic shift and obvious drop in the intensity of the main absorption peak was observed in the UV-vis spectrum when POM-2C$_{12}$ was added to the RhB starting solution in the dark (see discussion below). In this case therefore, the concentration of RhB during solar light illumination was determined using the absorption intensity at 565 nm, the position of the main RhB absorption peak observed after the addition of POM-2C$_{12}$.

Ag^+ reduction

Polyoxometalates can be reduced by organic electron donors (*e.g.*, alcohols) upon exposure to visible and ultraviolet light.[49] The *n*POM-TiO_2 hybrid material (0.02 g) was dispersed in isopropanol under stirring and illuminated by solar light for about 20 min. The colour of the dispersion changed from white to blue. An aqueous $AgNO_3$ solution (0.05 M) was added dropwise into the dispersion after removal from light, causing the blue-coloured dispersion to turn to brown abruptly. The brown powder was then filtered, washed with water and air-dried for TEM and EDX elemental mapping analysis.

Small angle neutron scattering

Data collection. Small Angle Neutron Scattering (SANS) experiments were performed on the LOQ SANS instrument[50] at the ISIS Neutron and Muon Spallation Source (Oxfordshire, UK) with a typical time-averaged flux of 2×10^5 cm^{-2} s^{-1}. The data were collected using a ^{3}He-CF_4 filled ORDELA "area" detector. The probed q range was approximately from 0.007 to 0.20 $Å^{-1}$, where q is the momentum transfer. The samples were measured in UV-spectrophotometer grade quartz cells with a path length of 1 mm at 25 °C.

The raw spectra were corrected for the background from the solvent, sample cell and other sources using standard workflows in the Mantid software package.[51] Scattering data were normalised against the scattering from a partially-deuterated polystyrene blend of known molecular weight to put the SANS data on an absolute scale,[52] so $I(q)$ equals the differential scattering cross section $d\sum/d\Omega(q)$. The output data was absolute scattered intensity, $I(q)$ in cm^{-1}, *versus* the momentum transfer, q in $Å^{-1}$.

Data modelling. The measured scattering intensity $I(q)$ as a function of the momentum transfer q, for centrosymmetric particles, is given as:

$$I(q) = A(\Delta\mathrm{SLD})^2 P(q) S(q, \phi) \quad (1)$$

where A is the scale factor. ϕ is the volume fraction of particles. ΔSLD corresponds to the scattering length density (SLD) contrast between particles and solvent. $P(q)$ is the form factor, which corresponds to the orientationally averaged scattering profile of a single particle and can be computed from a structural model. $S(q,\phi)$ is the structure factor that accounts for the interactions between the particles in the solution.

For a dilute suspension, the interactions between micelles, $S(q,\phi)$, can be neglected, so $I(q)$ mainly depends on the shape and size of the particles:

$$I(q) = A(\Delta\mathrm{SLD})^2 P(q) \quad (2)$$

Due to the large SLD difference between the POM-2C$_n$ headgroup (4.42×10^{-6} $Å^{-2}$) and tails (-0.38×10^{-6} $Å^{-2}$), the SANS patterns were fitted using core–shell models. For some of the scattering data, the core–shell sphere model[53] gave satisfactory fit results. However, in some circumstances, it gave an unusually large radius, which was not in accordance with the tail length of a surfactant monomer, so a core–shell ellipsoid model[54,55] was favoured and applied to get better fit results. In the modelling, the core of the micelles was assumed to only contain the hydrocarbon tails, while the shell was formed

from the headgroups, a partial contribution from the tails and water. Through fitting the form factor $P(q)$, the minimum radius of the core (R_{min}), shell thickness (t), core ellipticity (ε) and shell neutron scattering length density (SLD) were obtained.

In the semi-dilute regime, where micelles are interacting, the structure factor also has to be taken into account. Since the POM-2C$_n$ micelles are charged due to the ionisable headgroups, they experience a Coulomb repulsion modelled using the Hayter Penfold Rescaled Mean Spherical Approximation (RMSA)[56] which gives the volume fraction of charged particles interacting (ϕ) and the number of charges per micelle z (number of electrons). This model depends on the Debye screening length of interactions. This Debye length can be calculated knowing the temperature (25 °C) and the relative permittivity of the medium (72.08 for D_2O, 72.2 for 70 mol% D_2O).[57]

Scattering patterns from samples at the same concentration but in two different solvents (D_2O and 70 mol% D_2O) were fitted simultaneously using SasView (version 4.2.1) in order to better constrain the fits using contrast variation. Calculated neutron SLDs of the hydrocarbon tails, the POM headgroup and the solvents used for fitting are listed in ESI Table 1.†

Other Techniques

The electrical conductivities of the surfactant aqueous solutions were measured using a METTLER TOLEDO conductivity meter. NMR spectroscopic measurements were carried out using a 500 MHz Bruker Avance II+ spectrometer. Typical samples were made from POM-2C$_n$ surfactants dissolved in D_2O. The ^{31}P NMR was measured with a relaxation time of 20 seconds. IR spectra were measured using a Bruker IR spectrometer at room temperature in a dry box. TGA was applied to measure the change of sample weight as a function of temperature. An alumina crucible with about 100 mg of sample was put into a furnace, which was heated up in air at a constant heating rate of 1 °C min^{-1}, while a sensitive balance recorded sample weight loss. The results are displayed as the loss of mass percentage against temperature in °C. Analysis of carbon, hydrogen and nitrogen (CHN analysis) was carried out with a Carlo Erba 1112 elemental analyser at MEDAC Ltd Brunel Science Centre, Surrey, TW20 0JZ, UK. POM-2C$_n$ aqueous solutions at 5.5 mM were measured at room temperature using dynamic light scattering (DLS) in a Malvern Zetasizer Nano ZSP (Malvern, UK). All samples were filtered through a 0.45 μm filter (Millex-HA) to remove any dust before the measurements. Samples were measured at a scattering angle of 173° and a wavelength of 632.8 nm for 120 s, repeated 5 times. The size distribution, weighted in volume, was extracted using the CONTIN method. The zeta-potential of the micelles was also studied, at the same concentration, using the same instrument. Nitrogen sorption measurements were carried out at liquid nitrogen temperature (77.36 K) using a BELSORP instrument (BELSORP-mini Inc. Japan). The samples were degassed under vacuum at 523 K for 1000 min prior to the measurements. Surface areas were calculated using the Brunauer–Emmett–Teller (BET) equation. PXRD measurements were performed on a Stoe STADI P high-resolution system equipped with a DECTRIS Double MYTHEN 1K strip detector, and employing Cu-K$_{\alpha1}$ radiation (λ = 1.54060 × 10^{-10} m). The samples were measured in the range of 10° < 2θ < 70° at 2° per minute. The morphologies of the obtained materials were observed by TEM using a JEOL JEM-2100Plus instrument with an operating voltage at 200 kV maximum. An Oxford Instruments large area EDX detector, associated with the TEM, and Aztec analysis software were used for high-resolution elemental mapping analysis. Prepared POM-loaded mesoporous TiO_2 materials were characterised using an Anton Paar SAXSess instrument with a PANalytical PW3830 X-ray generator which gave a q range between 0.08 Å^{-1} and 2.7 Å^{-1}. The line X-ray source used was a Cu K$_\alpha$ X-ray tube at 40 kV and 50 mA. X-rays were detected by a reusable Europium excitation based image plate (size: 66 × 200 mm) with a 42.3 μm^2 pixel size. The image plate was subsequently read by a PerkinElmer cyclone reader using OptiQuant software. SAXS profiles were generated by using the SAXSquant program.

Kinetics of photocatalytic degradation

UV-vis absorption was used to follow dye degradation performed on a PerkinElmer Lambda 750S UV-vis spectrometer. The rate of photodegradation of rhodamine B (RhB) in the presence of photocatalysts can be calculated from a fit to the experimental data. The Langmuir–Hinshelwood model can be used to describe the kinetics of the photodegradation, and the model is further simplified if possible.[58] Here, the degradation kinetics were approximated as pseudo-first-order kinetics with respect to the concentration of RhB (C):

$$-\mathrm{d}C/\mathrm{d}t = k_{obs}C \quad (3)$$

where k_{obs} is the rate constant. Integration of the equation (with C_t, C_0 are the RhB concentrations at time t and 0 min respectively) gives:

$$\ln(C_t/C_0) = -k_{obs}t \quad (4)$$

where the values of k_{obs} (unit: min^{-1}) can be obtained directly from the regression analysis of a linear plot of $\ln(C_t/C_0)$ *versus* time.

Results and discussion

Characterisation of $K_6[\alpha\text{-}P_2W_{18}O_{62}]\cdot14H_2O$, $K_{10}[\alpha_2\text{-}P_2W_{17}O_{61}]\cdot19H_2O$ and POM-2C$_n$

POM-2C$_n$ surfactants with structure illustrated in Fig. 1 were prepared from $K_6[\alpha\text{-}P_2W_{18}O_{62}]\cdot14H_2O$, *via* the lacunary derivative $K_{10}[\alpha_2\text{-}P_2W_{17}O_{61}]\cdot19H_2O$ using established methods.[44]

Starting materials and POM-2C$_n$ (n = 12, 14, 16 and 18) were characterised by ^{31}P NMR (Fig. 2A–C and ESI Fig. 1†) and IR spectroscopy (Fig. 2D and ESI Fig. 2†). The ^{31}P NMR spectrum of $K_6[\alpha\text{-}P_2W_{18}O_{62}]\cdot14H_2O$ (Fig. 2A) shows the characteristic peak at −13.03 ppm, in addition to two small peaks at around −11.53 and −12.31 ppm, due to the $K_6[\beta\text{-}P_2W_{18}O_{62}]\cdot14H_2O$ isomer. After the modifications, two ^{31}P NMR peaks were

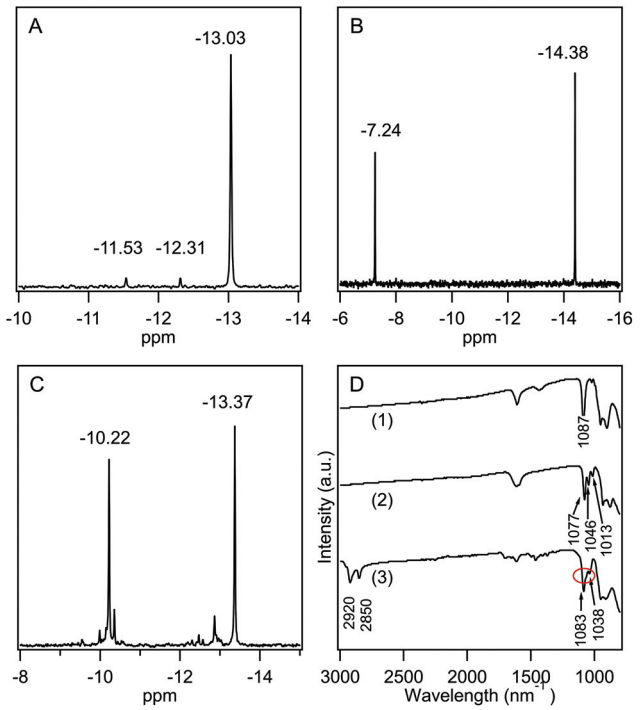

Fig. 2 ^{31}P NMR spectra of (A) $K_6[\alpha\text{-}P_2W_{18}O_{62}]\cdot 14H_2O$ (B) $K_{10}[\alpha_2\text{-}P_2W_{17}O_{61}]\cdot 19H_2O$ and (c) POM-$2C_{12}$. (D) IR spectra of (1) $K_6[\alpha\text{-}P_2W_{18}O_{62}]\cdot 14H_2O$ (2) $K_{10}[\alpha_2\text{-}P_2W_{17}O_{61}]\cdot 19H_2O$ and (3) POM-$2C_{12}$ (where the red circle indicates the existence of Dawson structured POM after tail grafting).

observed due to the non-equivalent phosphorus atoms both in the $K_{10}[\alpha_2\text{-}P_2W_{17}O_{61}]\cdot 19H_2O$ spectrum (−7.24 and −14.38 ppm, see Fig. 2B) and in the $K_6[P_2W_{17}O_{61}\{OSi_2(C_nH_{2n+1})_2\}]$ (Fig. 2C for POM-$2C_{12}$ and ESI Fig. 1† for POM-$2C_{14}$, POM-$2C_{16}$ and POM-$2C_{18}$). For the POM-$2C_{12}$ surfactant, C–H correlated NMR further suggests the successful grafting of the $C_{12}H_{25}$ hydrocarbon tails as shown in Fig. 3. The peak labelled 2 is due to diethyl ether impurities. Peaks labelled 1, 3 and 4 are correlated to the double hydrocarbon tails as illustrated in detail in Fig. 3. Carbon NMR spectra of POM-$2C_n$ with tail lengths $C_{14}H_{28}$, $C_{16}H_{33}$ and $C_{18}H_{37}$ are listed in ESI Fig. 3† and also evidence the presence of the hydrocarbon chain.

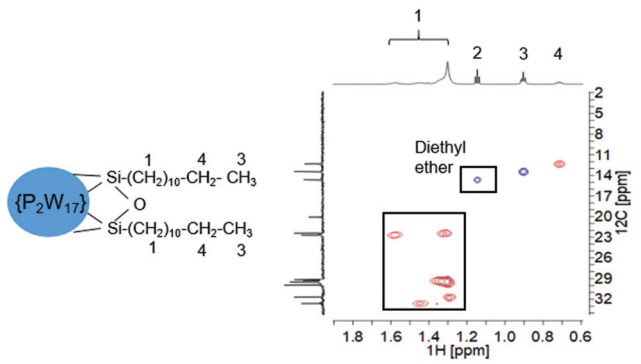

Fig. 3 C–H correlated NMR of POM-$2C_{12}$ illustrated by the POM-$2C_{12}$ molecular structure ({P_2W_{17}} represents {$P_2W_{17}O_{61}$}), the square on the left of the 2D NMR graph labelled 1 is related to the 10 methylene groups labelled 1 in the POM-$2C_{12}$ molecular structure. Blue signals represent methyl groups and red for methylene groups.

In the IR spectra (Fig. 2D), only one type of ν(P–O) was observed at 1087 cm^{-1} for symmetric $K_6[\alpha\text{-}P_2W_{18}O_{62}]\cdot 14H_2O$.[59,60] For $K_{10}[\alpha_2\text{-}P_2W_{17}O_{61}]\cdot 19H_2O$, the bands of ν(P–O) vibrations were observed at 1013, 1046 and 1077 cm^{-1}, similar to those reported in the literature.[61] After the attachment of the hydrocarbon tails to form the POM-$2C_{12}$ surfactant, the three ν(P–O) vibration peaks were retained with the peak at 1046 cm^{-1} overlapping with the peak at 1083 cm^{-1}. Peaks at 2920 and 2850 cm^{-1} correspond to the ν(C–H) vibration, indicating the presence of both {$P_2W_{17}O_{61}$} and hydrocarbon chains in the final product. IR spectra of POM-$2C_n$ (n = 14, 16 and 18) were obtained and are found to be similar to that of POM-$2C_{12}$, suggesting the presence of both polyoxometalate and hydrocarbon chain (see ESI Fig. 2†).

UV-vis absorbance spectra (ESI Fig. 4†), showed a bathochromic shift in the absorption edge upon attachment of the two hydrocarbon chains, so that the POM-$2C_{12}$ derivatives absorb light over a wider wavelength range compared to the lacunary $K_{10}[\alpha_2\text{-}P_2W_{17}O_{61}]\cdot 19H_2O$. TGA on the POM-$2C_n$ materials (ESI Fig. 5†), showed a mass loss of 6.73%, 7.00%, 7.13% and 10.05% corresponding to the tail weight percentage in POM-$2C_{12}$, POM-$2C_{14}$, POM-$2C_{16}$ and POM-$2C_{18}$ (calculated mass loss is 7.0%, 8.1%, 9.2% and 10.2% respectively). Additional CHN analyses suggest a carbon weight percentage of 7.11% and 7.84% and a hydrogen weight percentage of 1.56% and 1.66% in POM-$2C_{14}$ (C: 6.92%, H: 1.20%) and POM-$2C_{16}$ (C: 7.82%, H: 1.34%) respectively. The carbon weight percentages from CHN analyses give similar results to the calculated values. The deviation in H weight percentage between the theoretical and the experimental values may be attributed to moisture in the materials. These results confirm the successful synthesis and structural integrity of the POM-$2C_n$.

Critical micelle concentrations

ESI Fig. 6A–D† show plots of the electrical conductivity *vs.* the concentration of POM-$2C_n$ in water, and CMC values were determined by the intersections of the two straight lines. The CMCs of the POM-$2C_n$ surfactants *versus* hydrophobic chain length are plotted in Fig. 4, giving a trend similar to that observed for di-alkyl sulfosuccinate surfactants (CMCs given in ESI Table 2†),[62,63] alkyl trimethylammonium bromides (abbreviated as C_nTAB, CMC values given in ESI Table 3†)[64,65] and sodium alkyl sulfates (CMC values in ESI Table 4†),[66–70] where a surfactant with longer hydrophobic tail/tails has a lower CMC compared to the one with the same headgroup but shorter hydrophobic part.

Degree of micelle ionisation and free energy of micellisation

The percentage of bound counterions in relation to the number of surfactant ions in the micelles is the fraction of micellar charge neutralized, β, defined as counterion binding.

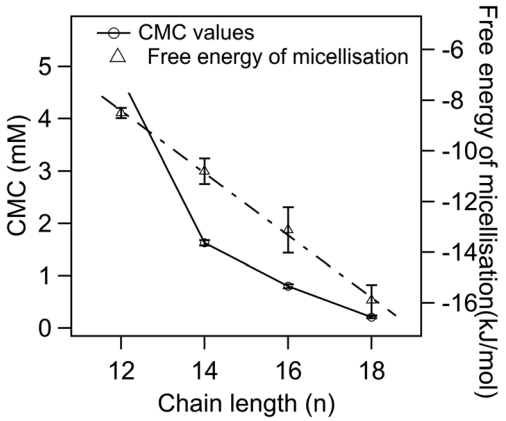

Fig. 4 Plot of CMC and free energy of micellisation (ΔG°_{mic}) *vs.* hydrocarbon chain length. The solid line through the CMC values is a guide to the eye. The dashed line is a linear fit to the free energies of micellisation.

The degree of micelle ionisation α equals $1-\beta$, and can be calculated from measurements of conductivity with concentration from the slope measured above the CMC (m_1) divided by that below the CMC (m_2): $\alpha = m_1/m_2$.[71] The calculated α values are listed in Table 1. It can be seen that micelles formed by POM-2C$_n$ with longer tails have a lower counterion dissociation, therefore higher screening by the counterion. The POM-2C$_n$ surfactants show similar changing trends in α as seen for traditional surfactants, such as di-alkyl sulfosuccinates, C$_n$TAB and sodium alkyl sulfates (ESI Tables 2–4†).[62,64,65,68,69,72] The counterion binding β and the CMC are related to the free energy of micellisation *via* equation:

$$\Delta G^{\circ}_{mic} = (1+\beta)RT\ln(\mathrm{CMC}) \quad (5)$$

the calculated free energies of micellisation are listed in Table 1 and plotted in Fig. 4. The ΔG°_{mic} was calculated to be between −8.5 and −15.9 kJ mol^{-1} at room temperature. The linear relationship in the variation of ΔG°_{mic} with the tail length is consistent with that observed for C$_n$TAB surfactants.[73] The value of the slope obtained from the line in Fig. 4, −1.26 ± 0.05 kJ mol^{-1}, here represents the free energy increment for two CH$_2$ groups (designated as ΔG°_{t}). The ΔG°_{t} of the POM-2C$_n$ system is much lower than that of C$_n$TAB (−3.45 ± 0.2 kJ mol^{-1}) with a single hydrocarbon tail.[73]

By comparing the ΔG°_{mic} values of POM-2C$_n$ with those of di-alkyl sulfosuccinate surfactants (ESI Table 2†), it is seen that the POM-2C$_n$ surfactants can form micelles more easily in water because they have longer hydrophobic tails. They also have relatively similar free energies of micellisation[65] with those of single-tailed C$_n$TAB (n = 12, 14, 16) surfactants (ESI Table 3†). These results indicate that, despite the fact that POM-2C$_n$ are double-tailed surfactants, they form micelles as easily as conventional single-tailed surfactants and aggregate more efficiently compared to conventional anionic double-tailed surfactants.

Table 1 The degree of micelle ionisation and free energy of micellisation values of POM-2C$_n$ in water, errors were calculated from those from the determination of CMCs

Material	CMC (mM)	α	ΔG°_{mic} (kJ mol^{-1})
POM-2C$_{12}$	4.78 ± 0.08	0.53 ± 0.04	−8.5 ± 0.2
POM-2C$_{14}$	1.63 ± 0.05	0.44 ± 0.03	−10.8 ± 0.5
POM-2C$_{16}$	0.80 ± 0.04	0.29 ± 0.03	−13.1 ± 0.9
POM-2C$_{18}$	0.21 ± 0.02	0.26 ± 0.02	−15.9 ± 0.6

SANS study of POM-2C$_n$

Above their CMCs, the POM-2C$_n$ surfactants assemble in water. The shape of these aggregates is expected to have important influences in the field of micellar catalysis,[74] photochemistry[75] and materials templating,[76] and is therefore interesting to investigate. We used SANS to probe the micelles formed by these surfactants in aqueous solutions.

The best fit for the micelles formed by POM-2C$_{12}$ in water was obtained from a core–shell ellipsoidal model. The SANS patterns and their corresponding fits are plotted in Fig. 5 for the D$_2$O contrast, while the fitted parameters along with the definition of the abbreviations are listed in Table 2. The elongation of the micelles was found to be dependent on the concentration: the ellipticity, ε, indicating the degree of elongation, varies from 4.0 ± 0.4 to 5.1 ± 0.4. Similarly, R_{min} ranges from 11 ± 1 Å to 15 ± 1 Å, slightly below the length of fully extended C$_{12}$H$_{25}$ chains according to the Tanford equation (16.7 Å).[77] Measurements of solutions prepared using 70 mol% D$_2$O as solvent (a value that was calculated to contrast match the POM-2C$_n$ headgroup) were also made (ESI Fig. 7A†). Fitting the data at 70 mol% D$_2$O still required a shell in the model, but with a lower SLD than that calculated for both dry POM and solvent (ESI Table 5†), suggesting that a portion of the hydrocarbon tail is present in the shell. The shell thickness was found to decrease with increasing concentration (from 22 ± 1 Å at 16.6 mM to 13 ± 1 Å at 99.1 mM). Except for the lowest concentration, these values (see Table 2) are in the same range as the dry {P$_2$W$_{17}$O$_{61}$} headgroup size (between 12 and 17 Å due to the ellipsoidal shape of the headgroup).[78]

With increasing concentration, a broad peak emerged at around q = 0.06 Å^{-1}. The peak indicates the intermicellar inter-

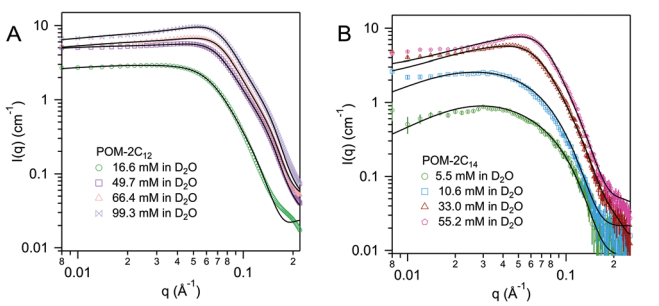

Fig. 5 SANS patterns of (A) POM-2C$_{12}$ and (B) POM-2C$_{14}$ micelles in D$_2$O at different concentrations. The fits are given as black lines.

Table 2 Fitted core–shell ellipsoidal model parameters[a] for POM-2C_{12} and POM-2C_{14} micelles in D_2O

Conc. (mM) (±0.1)	R (Å) (±1)	ε	t (Å) (±1)	z (e) (±0.5)	SLD ($\times 10^{-6}$ Å^{-2}) (±0.2)	ϕ (±0.005)
POM-2C_{12}						
16.6	11	4.5 ± 0.3	22	1.0	5.3	0.096
49.7	12	4.6 ± 0.3	16	1.0	5.0	0.140
66.4	12	5.1 ± 0.4	15	1.3	4.6	0.153
99.1	15	4.0 ± 0.4	13	1.5	4.8	0.160
POM-2C_{14}						
5.5	17	1.9 ± 0.3	15	4.4	5.1	0.011
10.6	17	2.1 ± 0.3	18	3.7	5.3	0.034
33.0	18	2.0 ± 0.3	18	3.6	5.3	0.094
55.2	17	2.1 ± 0.2	18	4.3	5.0	0.137

[a] R_{min}, the minimum radius of the core; R_{max}, the maximum radius of the core; ε, R_{max}/R_{min} (ellipticity); ϕ, volume fraction; SLD, neutron scattering length density; t, shell thickness; z, micellar surface charge.

actions and was fitted using the RMSA model. The fits show a moderate increase in the charge per micelle with increasing concentration. The value for the charge on the micelle (around 1e) is surprisingly low given the potential −6 charge available to the headgroup, suggesting that although the conductivity results indicate that counterion dissociation is relatively high at the CMC, it becomes much lower above the CMC.

POM-2C_{14} also forms ellipsoidal micelles in water according to the modelling of the SANS patterns given in Fig. 5B (D_2O contrast) and ESI Fig. 7B† (70 mol% D_2O contrast). Fit parameters associated with the form factor of POM-2C_{14} micelles were found to have little dependence on the surfactant concentration (see Table 2). These micelles were less elongated compared to their POM-2C_{12} counterparts, with an ellipticity of *ca.* 2.0. R_{min} was found around 17–18 Å, again slightly smaller than the size of the fully extended $C_{14}H_{29}$ chain (19.2 Å) estimated by the Tanford equation.[77] The hydrated shell thicknesses were found to be 15 ± 1 Å at 5.5 mM and 18 ± 1 Å for higher concentrations, which lies in the size range (12–17 Å) of $\{P_2W_{17}O_{61}\}$.[78] The difference in shell thickness between 5.5 mM and the other concentrations is probably due to the weak signal at this low concentration. Increasing concentration also results in electrostatic repulsion arising between micelles, evidenced by a broad peak in the SANS patterns, however, this time a higher micelle surface charge was seen (3.6–4.4e).

For both POM-2C_{16} and POM-2C_{18}, the fitting of the SANS patterns suggests the formation of spherical micelles in water, rather than ellipsoidal micelles (see Fig. 6 and ESI Fig. 8†). The radius of the spherical micelles (R) was found to be around 20 and 22 Å respectively. Shell thickness was around 19 Å for POM-2C_{16}, and 17 Å for POM-2C_{18} (see Table 3 and ESI Table 6†). Similar to POM-2C_{14}, an increase in the concentration resulted in an increase in the intermicellar interactions, modelled by an increase in the volume fraction ϕ. The surface charge was found to be around 4.2e for POM-2C_{16}, and around 5.2e for POM-2C_{18}. Although in general, the fit reproduced the data well, it was observed to fail to reproduce the scattering at the lowest angles for the 70 mol% D_2O solution at high concentrations (see ESI Fig. 8†), probably caused by a small amount of large aggregates observed in these samples.

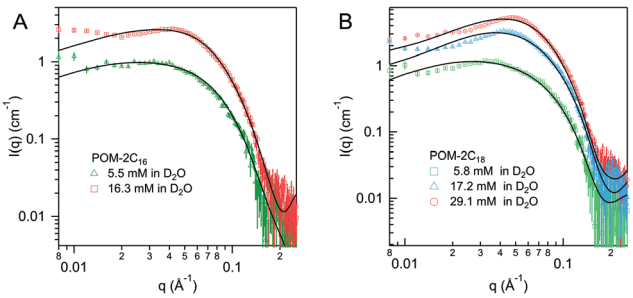

Fig. 6 SANS patterns of (A) POM-2C_{16} and (B) POM-2C_{18} micelles in D_2O at different concentrations. The fits are given as black lines.

Table 3 Fitted core–shell model parameters[a] for POM-2C_{16} and POM-2C_{18} micelles in D_2O

Conc. (mM) (±0.1)	R (Å) (±1)	t (Å) (±1)	z (e) (±0.2)	SLD ($\times 10^{-6}$ Å^{-2}) (±0.5)	ϕ (±0.005)
POM-2C_{16}					
5.5	20	19	4.2	5.6	0.019
16.3	22	19	4.3	5.7	0.053
POM-2C_{18}					
5.8	22	17	4.9	5.6	0.015
17.2	22	17	5.5	5.5	0.049
29.1	22	17	5.2	5.3	0.077

[a] R, the radius of the core; ϕ, volume fraction; SLD, neutron scattering length density; t, shell thickness; z, micellar surface charge.

From the SANS fitting, an increase in the radius of the micelles (comparing R_{min} for ellipsoids and R for spheres) was observed with increasing hydrophobicity of the surfactant, in agreement with observations made for commercial C_nTAB surfactants and sodium alkyl sulfates.[64,67] Moreover, the tail length strongly influences the shape of the micelles, with an obvious change from an ellipsoid to a sphere as the hydrocarbon tail of the surfactants becomes longer. As illustrated in Fig. 7, POM-2C_{12} and POM-2C_{14} both form ellipsoid micelles in aqueous solutions, however, the ellipticity of POM-2C_{14} (around 2) is less than half of that of POM-2C_{12} (around 4.5),

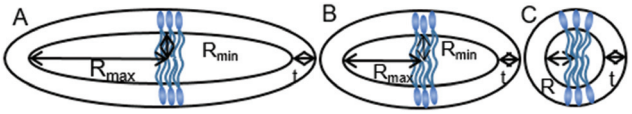

Fig. 7 Schematic representation of the POM-2C$_n$ micelle shapes (A) POM-2C$_{12}$ (B) POM-2C$_{14}$ (C) POM-2C$_{16}$ and POM-2C$_{18}$ where t is the shell thickness, R_{max} and R_{min} are the maximum and minimum of core radius in an ellipsoidal micelle model, and R is the core radius of the spherical micelle.

while both POM-2C$_{16}$ and POM-2C$_{18}$ form spherical micelles. In contrast, commercial single-tailed surfactants, such as C$_n$TAB and sodium alkyl sulfates, undergo an increase of the micelle ellipticity with increased tail length (see the calculated ellipticity listed in ESI Tables 3 and 4† using the information provided by references).[64,67]

For the POM-C$_n$ surfactants, the theoretical packing parameters, calculated for different tail lengths but assuming the same equilibrium area per molecule (the cross-sectional area of the headgroup estimated according to the size of the headgroup,[78] 124.3 Å^2), lies close to the 1/3 limit between spherical and rod-like micelles, without any clear trend explaining the experimental data. This suggests that the equilibrium area per molecule may be different between them due to the difference in the repulsion between the surfactant headgroups. Considering the repulsive interactions, as listed in Tables 2 and 3, the surface charge increases with the tail length which may induce a larger equilibrium area per molecule. Therefore the packing parameter (= v/al, where, a is the equilibrium area per molecule, v is the hydrophobic tail volume and l is the hydrophobic tail length, the volume-to-length ratio v/l of the tail is independent of the tail length for common surfactants) decreases with increased tail length, giving a value under 1/3, which predicts the formation of spherical micelles.[79] This is consistent with the SANS results where longer tailed surfactants form more globular micelles.

Dynamic light scattering (DLS) was used to detect the hydrodynamic radius distributions of the micelles, shown in Fig. 8A. The singular peak in the DLS volume-weighted size distribution results suggests that there is only one population of micelles in each solution. An increase in size obtained from DLS is observed with tail length, $C_{14}H_{29}$, $C_{16}H_{33}$ and $C_{18}H_{37}$ give a hydrodynamic radius of 31 ± 5, 41 ± 5, and 48 ± 5 Å respectively, in agreement with the increase of micellar size observed from SANS fitting results. It is noted that the size of the POM-2C$_{12}$ micelles (48 ± 5 Å) probed by DLS is relatively larger compared to those of POM-2C$_{14}$ and POM-2C$_{16}$ micelles, likely due to their ellipsoidal shape, which is not taken into account in DLS analysis. The POM-2C$_n$ micelles exhibit strongly negative surface charges as evidenced by their zeta-potentials (see Fig. 8B), giving similar results to the conductivity measurements (longer-tailed surfactant forms micelles with less charged surfaces), but opposite trend to the micelle charge information obtained from SANS fitting. The reason for the opposite trend between SANS results and zeta-potentials remains unclear at this stage.

POM-TiO$_2$ materials synthesised using POM-2C$_n$ micelles as templates

Catalysts were prepared by mixing POM-2C$_n$ (n = 12, 16 and 18) with titania precursor in acidic solution, followed by a hydrothermal treatment, filtration and calcination at 500 °C to remove the organic $2C_nH_{2n+1}$ chains from the material (see TGA analysis of the POM-2C$_{12}$ in ESI Fig. 5A,† showing the organic part is burnt away). Several studies have demonstrated that the Wells–Dawson structure remains stable up to 600 °C,[45–47] so it is expected to remain intact during calcination. Transmission electron microscopy (TEM) images of the 12POM-TiO$_2$ material (Fig. 9A) show aggregates of small spherical particles. A higher resolution image focusing on a selected area of the 12POM-TiO$_2$ material, made *via* HRTEM (Fig. 9B), clearly shows lattice fringes which indicate an ordered crystalline structure of the TiO$_2$. Although the $\{P_2W_{17}O_{61}\}$ units have a very small size and a low concentration in the material (Table 4), they can be seen as black dots in the HRTEM micrograph because of their high electron density. Several of these dots are highlighted using green dashed circles in Fig. 9B.

EDX elemental mapping analysis also evidences the presence of the POM units within the hybrid material. The

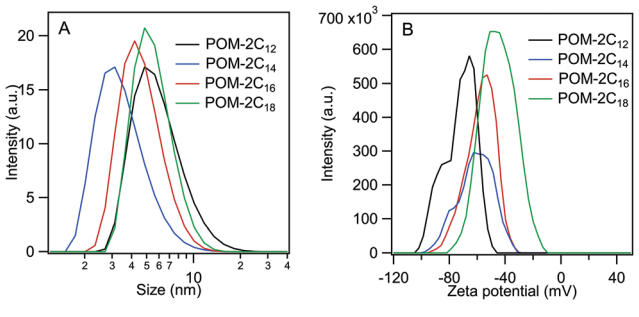

Fig. 8 (A) Volume-weighted size distributions (obtained *via* the CONTIN method) and (B) zeta-potentials of 5.45 mM POM-2C$_n$ solutions (n = 12, 14, 16 and 18).

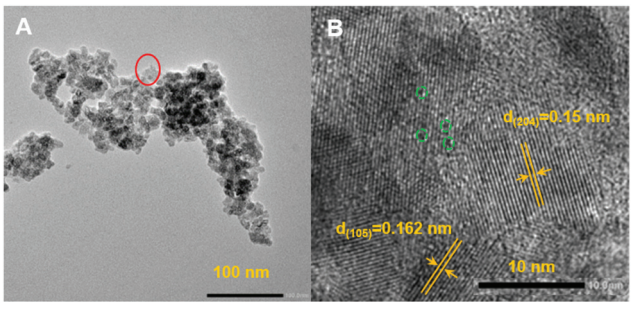

Fig. 9 (A) TEM and (B) HRTEM micrographs of the 12POM-TiO$_2$ material. HRTEM micrograph in (B) is a zoom from the region indicated with a red circle in (A). The dashed green circles in (B) are the possible locations of POMs in the 12POM-TiO$_2$ material.

Table 4 Ti : W atomic ratios obtained from EDX analysis, surface areas obtained from BET annalysis and mean pore sizes

Material	Ti : W	Surface area (m^2 g^{-1})	Mean pore size (nm)
12POM-TiO_2	122 : 1	191 ± 8	6.4 ± 0.5
16POM-TiO_2	154 : 1	165 ± 8	5.3 ± 0.6
18POM-TiO_2	169 : 1	148 ± 5	6.2 ± 0.4
16POM-TiO_2-2	12 : 1	179 ± 5	5.0 ± 0.6
TiO_2	—	99 ± 5	8.3 ± 0.4

element distributions of the 12POM-TiO_2 associated with the TEM image in Fig. 9A, are given in ESI Fig. 9.† It was clear that both W and Ti elements are uniformly distributed within the material, suggesting the existence of POMs within the hybrid material.

To verify the structural integrity of the Dawson structure of the POMs within the material, IR spectroscopy of the 12POM-TiO_2 material was attempted (see ESI Fig. 10†). Due to the small amount of POMs in the material (Ti : W = 122 : 1, see Table 4), the characteristic peaks of Dawson structured POM were observed as a single broad peak at *ca.* 1080 nm^{-1} in the IR spectrum.

Reduced POMs are known to reduce metal ions *in situ* to metal nanoparticles. Therefore, to corroborate the preservation of POM units within the porous TiO_2,[80] the photocatalytic reduction of Ag^+ was carried out. Experimental details can be found in the Experimental section. EDX elemental mapping analysis was applied to the collected brown product, and the Ag element distribution is shown in ESI Fig. 11B,† suggesting that Ag nanoparticles are present in the product. This indicates that POM units are present and are chemically active.

The PXRD patterns of SDS templated TiO_2, 12POM-TiO_2, 16POM-TiO_2 and 18POM-TiO_2 materials (Fig. 10) demonstrate the characteristic diffraction peaks of anatase TiO_2 (space group: *I*41/*amd*, JCPDS no. 21–1272). We found no diffraction evidence for the POM phase (see ESI Fig. 12†), since the POM within the TiO_2 are dispersed but not crystallised. This is also seen in the PXRD pattern of dried POM-2C_{12} surfactant which also shows no diffraction peak (see ESI Fig. 13†). Small angle X-ray scattering showed no long-range ordering of the pores within the SDS templated TiO_2 or the *n*POM-TiO_2 materials (see ESI Fig. 14†).

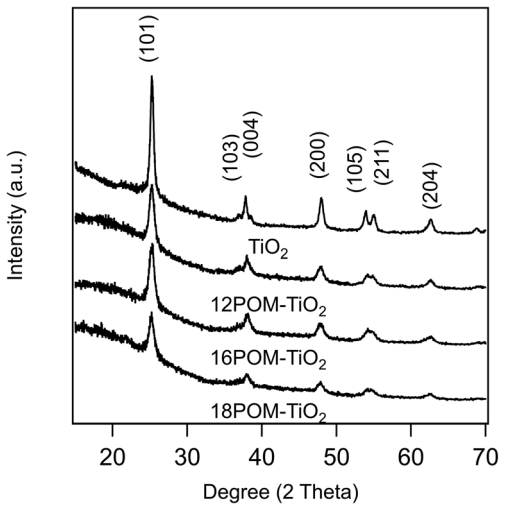

Fig. 10 PXRD patterns of *n*POM-TiO_2 materials (*n* = 12, 16 or 18).

Both SDS templated TiO_2 and *n*POM-TiO_2 materials show a type IV nitrogen sorption isotherm (see ESI Fig. 15A†). The resulting *n*POM-TiO_2 materials have relatively high surface areas, listed in Table 4 along with their mean pore diameters (pore size distributions are illustrated in ESI Fig. 15B†). *n*POM-TiO_2 materials have smaller mean pore sizes compared to SDS templated TiO_2 due to the occupation of POMs within the pores. The mean pore diameter of 12POM-TiO_2 material lies between the minimum size ($2R_{min}$ = 2.2 nm) and the maximum size ($2R_{max}$ = 9.9 nm) of the POM-2C_{12} micelles. The 16POM-TiO_2 and 18POM-TiO_2 materials have slightly larger mean pore sizes compared to their corresponding micellar diameter (4.0 and 4.4 nm). Larger pores (around *ca.* 60–100 nm) were also observed in 12POM-TiO_2, which contribute to this sample having the largest surface area among *n*POM-TiO_2 materials. The mean pore size of the 18POM-TiO_2 material is about 17.5% larger in comparison to 16POM-TiO_2, which demonstrates the tunability of the pore size through using larger spherical micelles as soft templates.

To evaluate the effect of the POM surfactant concentration on the structural properties of the material, a second TiO_2 material was prepared using POM-2C_{16} at a higher concentration (22.0 mM) and labelled 16POM-TiO_2-2. EDX elemental mapping shows the presence of POM in the 16POM-TiO_2-2 (see ESI Fig. 16†). The POM content in 16POM-TiO_2-2, indicated by the Ti : W ratio listed in Table 4, is much higher than for 16POM-TiO_2. This suggests that the amount of POM in the hybrid materials can be tuned by the concentration of the POM-2C_n used in the preparation solution. No diffraction peaks are observed in the SAXS pattern (ESI Fig. 17†), again suggesting no long-range organisation of the pores. The 16POM-TiO_2-2 material has a slightly higher surface area compared to 16POM-TiO_2 (179 m^2 g^{-1} *versus* 169 m^2 g^{-1}) and a relatively smaller mean pore size (5.0 nm *versus* 5.3 nm), parameters given in Table 4. The sorption isotherm of 16POM-TiO_2-2 (ESI Fig. 18†) shows a more obvious hysteresis loop than for 16POM-TiO_2, indicating the presence of more well defined mesopores.

Photocatalytic properties

Dawson structured $\{P_2W_{17}O_{61}\}$ was chosen as the focus of this work for its photocatalytic properties. The photoabsorption of 12POM-TiO_2 in the range of 250–800 nm shows an absorbance shoulder for wavelengths between *ca.* 400 and 700 nm (ESI Fig. 19A†). The 12POM-TiO_2 possesses a bandgap at around 3.3 eV (obtained by plotting $(Ah)^2$ as a function of the energy), similar to that of TiO_2 (ESI Fig. 19B†).[81] The band gap does not change after the decoration of TiO_2 with POM, however, the resulting material now shows absorbance in a wavelength range where TiO_2 normally would not absorb.[82,83]

The photocatalytic properties of the *n*POM-TiO_2 materials were tested *via* the degradation of RhB during irradiation of these materials with solar light (see for example ESI Fig. 20A†). Their photocatalytic behaviours were compared to SDS templated TiO_2 which has a surface area of *ca.* 99 m^2 g^{-1}. The *n*POM-TiO_2 (n = 12, 16 and 18) materials showed higher activities than that of the SDS templated TiO_2 (Fig. 11A). The photodegradation properties of the POM amphiphiles alone, compared to the POMs supported within the 12POM-TiO_2 material were evaluated under the same conditions, by using the same number of moles of POM-$2C_{12}$ as that of the POM species in 0.015 grams of 12POM-TiO_2. A bathochromic shift and an obvious drop in the intensity of the main absorption peak were observed in the UV-vis spectrum of RhB (see ESI Fig. 20B†) after POM-$2C_{12}$ was added to the starting solution (RhB, 0.031 mM; H_2O_2, 1.5 mM). This shift in the spectrum has been previously reported and can be explained by strong electrostatic interactions between RhB molecules with the negatively charged polyoxometalate species.[84,85] Due to the shift in the spectrum, the concentration of RhB in this solution was determined using the absorption intensity at 565 nm rather than at 553 nm as for the *n*POM-TiO_2 materials. As seen in Fig. 11A, around 11% of RhB was decomposed by POM-$2C_{12}$ in 80 min, which is *ca.* one-tenth of the amount that the equivalent amount of POM within 12POM-TiO_2 decomposed over the same time. These results suggest a synergistic effect between POMs and TiO_2 in the *n*POM-TiO_2 materials that we prepared.

Among the *n*POM-TiO_2 materials, the 12POM-TiO_2 exhibited the best degradation performance, with almost 80% of the RhB degraded after 20 min. 16POM-TiO_2 and 18POM-TiO_2 were less effective in the first 20 min, decomposing *ca.* 65% and 45% of RhB respectively. The degradation rates fit a first-order model well. The slope of a linear plot of ln (C_t/C_0) *versus* irradiation time gives the apparent degradation rate constant (Fig. 11B). The obtained fitting parameters related to the kinetics, apparent degradation rate constant k_{obs} and correlation coefficient r, are listed in Table 5. There is an obvious rate enhancement of *n*POM-TiO_2 compared to porous TiO_2, increasing from 0.0096 to 0.0513 min^{-1}. Correlation coefficients, r, are found to be between 0.9683 and 0.9910, indicating the excellent linear response in the studied range of concentrations.

Table 5 Kinetic parameters obtained from the fitting of the experimental results in Fig. 11B

Material	k_{obs} (min^{-1})	r
12POM-TiO_2	0.0513 ± 0.0016	0.9683
16POM-TiO_2	0.0414 ± 0.0008	0.9799
18POM-TiO_2	0.0367 ± 0.0003	0.9910
TiO_2	0.0096 ± 0.0003	0.9708

The Ti to W atomic ratio in each material obtained from EDX elemental mapping analysis is listed in Table 4. The 12POM-TiO_2 hybrid material has a relatively higher W content compared to 16POM-TiO_2 and 18POM-TiO_2, and also had the highest POM content in the materials synthesised at this POM amphiphile concentration. The value of k_{obs} decreases as the amount of POM present in the *n*POM-TiO_2 materials decreases. Therefore, besides the high surface area induced by the surfactant templating, the higher POM content of the prepared 12POM-TiO_2 also contributes to its outstanding properties in RhB photodegradation compared to the other materials studied here.

When the ratio of POM to TiO_2 was increased, in the 16POM-TiO_2-2 compared to 16POM-TiO_2, the degradation of RhB was completed more rapidly than when 16POM-TiO_2 was used (60 min *versus* 80 min as shown in ESI Fig. 21†). This suggests the possibility of tuning the photocatalytic properties of the hybrid materials through altering the POM content.

Furthermore, the RhB photodegradation activity of 12POM-TiO_2 is still remarkably high after eight continuous photo-catalytic cycles (see Fig. 12). The complete photodegradation of RhB is still obtained after 80 min at the 8th cycle, while there is a slight decrease of the amount of RhB degraded after 20 min (*ca.* 70% *versus* 80% for the 1st cycle). The PXRD pattern of 12POM-TiO_2 after 8 cycles indicates an anatase phase (ESI Fig. 12†), equivalent to that in the fresh

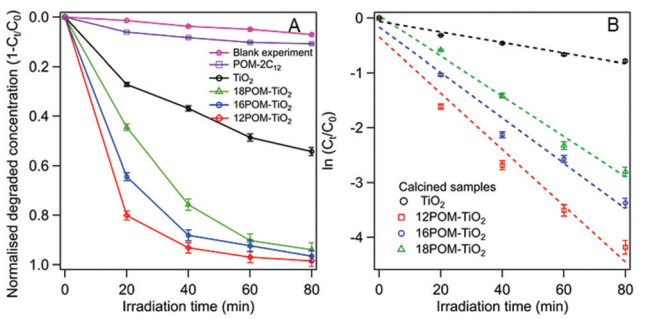

Fig. 11 (A) Plot of normalised degraded concentration of RhB, 1 – C_t/C_0, in the presence of different catalysts *versus* irradiation time. A blank measurement was recorded for comparison. (B) Plot of ln(C_t/C_0) against irradiation time, C_t and C_0 are the RhB concentrations at time t and 0 min respectively.

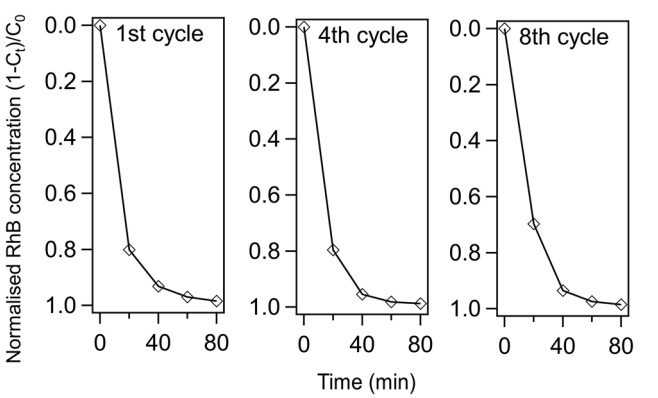

Fig. 12 Performance of 12POM-TiO_2 in RhB degradation over several cycles.

material, showing the stability of the TiO_2 structure over several cycles.

The photocatalytic pathway can be summarised as follows:[39,86] (1) the electrons are excited from the valence band (VB) to the conduction band (CB) of TiO_2 under UV irradiation. (2) The electrons at the CB of TiO_2 transfer to the POMs. Furthermore, POMs are photo-excited simultaneously and the electrons from both the CB of TiO_2 and the photoexcitation of POMs accumulate together on the POMs to form charge-transfer excited POMs (designated as POMs*). (3) POMs* transfer electrons to oxygen in the solution to form reactive oxygen species, while photoexcited holes react with water to form $^{\bullet}OH$ radicals, and (4) these radicals are involved in the process of photodegradation. POMs have been proven to enhance the photocatalytic properties of TiO_2 in several studies,[38,39] since they efficiently reduce the recombination rate of photoexcited holes and electrons in TiO_2. Therefore, step (1) is enhanced. Step (2) is accelerated here due to the intimate contact between POMs and TiO_2 given by the synthesis method. Moreover, POMs not only behave as charge separators in the hybrid materials but also photocatalysts that contribute to the photodegradation. Furthermore, the electrostatic interaction between oppositely charged POMs and RhB molecules also reinforces step (4). Overall, the decorating POMs speed up the degradation efficiency due to their rapid transportation of electrons, their ability to decrease the recombination rate of electron–hole pairs and their intrinsic photocatalytic properties, rather than by narrowing the band gap.

Chen, *et al.*[39] have studied the photocatalytic degradation of 2,4-dichlorophenol by $PW_{12}O_{40}^{3-}/TiO_2$ prepared by physical mixing, and the performance was improved by nearly 20% within the first 50 min when 0.8 mM $PW_{12}O_{40}^{3-}$ was present. This method, however, limits the recyclability of the $PW_{12}O_{40}^{3-}$ due to its solubility in water. Photodegradation of 1,2-dichlorobenzene using systems of TiO_2 and polyoxometalates ($PW_{12}O_{40}^{3-}$, $SiW_{12}O_{40}^{4-}$ or $W_{10}O_{32}^{4-}$) were studied by Ozer and co-workers.[87] The addition of POM anions into the TiO_2 suspension resulted in a significant rate enhancement, with $PW_{12}O_{40}^{3-}$ the most effective anion. The rate constant reached a limit of 0.03 min^{-1}, 600% greater than pure TiO_2 system, when the addition of $PW_{12}O_{40}^{3-}$ was at *ca.* 0.15 mM. In comparison to our work, the degradation rate constant of 12POM-TiO_2 is 0.051 min^{-1}, which is around 500% greater than that of the SDS templated TiO_2 material (0.0096 min^{-1}), while, importantly our materials also provide recyclability. Pearson *et al.* conducted a series of studies on materials obtained by loading $H_3P_{12}W_{12}O_{40}$ onto TiO_2 nanoparticles or TiO_2 nanotubes as a co-catalyst.[40,88,89] The degradation of Congo red dye was improved by around 14% compared to the original TiO_2 within the first 30 min.[40,89] However, the recyclability of the materials was not studied.

Thus, our system enables an improvement in photodegradation properties as well as providing improved recyclability, with photocatalytic performance maintained for at least eight continuous photo-catalysis cycles, compared to the addition of polyoxometalates into a TiO_2 suspension or the previous studies discussed above. The POM content in the POM-TiO_2 materials can be tuned through varying the concentration of POM amphiphiles. This synthesis method provides a stronger anchoring of polyoxometalates within the hybrid material and intimate contact between the polyoxometalates and TiO_2, ensuring their stability during use, easy recovery and reuse of the materials.

Conclusion

Novel surfactants with inorganic $\{P_2W_{17}O_{61}\}$ POM as headgroups and double-hydrocarbon chains (C_{12}, C_{14}, C_{16} or C_{18}) were successfully synthesised. The micelle morphologies were studied using SANS to reveal core–shell structures. The shape of the micelles can be tuned by changing the length of the hydrophobic tails, such that surfactants with longer hydrophobic tails tend to form less elongated and more globular micelles. Moreover, SANS evidenced strong interactions due to Coulomb repulsion between negatively charged micelles. These data were supported by DLS and zeta-potential measurements. The micelles were used to template TiO_2 through a hydrothermal method to form, after calcination, *n*POM-TiO_2 hybrid catalysts (n = 12, 16 or 18). Through this method, the $\{P_2W_{17}O_{61}\}$ units, as an excellent electron acceptor, an electron transport material and a photocatalyst, were incorporated into the porous titania materials. The photocatalytic properties of the *n*POM-TiO_2 hybrid materials were tested by the photodegradation of aqueous RhB solution as a model reaction. The results reveal that the *n*POM-TiO_2 photocatalysts possess enhanced photodegradation properties in comparison with SDS templated TiO_2, confirming their superior photocatalytic activity. The rate constants of the photodegradation extracted here were found to be almost 5 times higher for the 12POM-TiO_2 materials compared to porous TiO_2 templated by SDS. This study demonstrates the highly promising use of POM-2C_n amphiphiles as templating agents in the synthesis of porous POM-TiO_2 hybrid catalyst, having well-dispersed polyoxometalates within a porous anatase TiO_2 matrix. Using the same method, it is possible to increase the polyoxometalate content in the material by using a higher concentration of the initial surfactant solution. Furthermore, other metal oxide materials loaded with polyoxometalates could be synthesised using similar methods, offering a flexible and straightforward approach to harness the functionality of polyoxometalates in porous materials for catalysis.

Conflicts of interest

There are no conflicts to declare.

Acknowledgements

A. Di. thanks University of Bath and China Scholarship Council for supporting her Ph.D studies. The authors would

like to thank the ISIS Neutron and Muon Source for the award of beam time (experiment no. RB1720185, DOI: 10.5286/ISIS.E.RB1720185). We acknowledge assistance from Andrew P. Golightly in developing POM amphiphile synthesis routes, and RJE thanks EPSRC, Johnson Matthey (Synetix) and ICI (Uniqema) for an Industrial CASE Award to APG (GR/P02066/01). The authors gratefully acknowledge the Material and Chemical Characterisation Facility (MC^2) at University of Bath (DOI: 10.15125/mx6j-3r54) for technical support and assistance in this work. This work benefited from the use of the SasView application, originally developed under NSF award DMR-0520547. SasView contains code developed with funding from the European Unions Horizon 2020 research and innovation programme under the SINE2020 project, grant agreement No. 654000. The data supporting this work has been uploaded to the University of Bath Research Data Repository and is accessible at DOI: 10.15125/BATH-00931.

References

1 Y. F. Song, D. L. Long, C. Ritchie and L. Cronin, *Chem. Rec.*, 2011, **11**, 158–171.
2 M. T. Pope and A. Müller, in *Introduction to polyoxometalate chemistry: from topology via self-assembly to applications*, Springer, 2001, pp. 1–6.
3 Q. Fang, J. Fu, F. Wang, Z. Qin, W. Ma, J. Zhang and G. Li, *New J. Chem.*, 2019, **43**, 28–36.
4 Y. Chen, S. Tian, Z. Qin, J. Zhang, Y. Cao, S. Chu, L. Lu and G. Li, *Nanoscale*, 2019, **11**, 22270–22276.
5 B. Keita, G. Zhang, A. Dolbecq, P. Mialane, F. Sécheresse, F. Miserque and L. Nadjo, *J. Phys. Chem. C*, 2007, **111**, 8145–8148.
6 S. Gao, R. Cao, J. Lü, G. Li, Y. Li and H. Yang, *J. Mater. Chem.*, 2009, **19**, 4157–4163.
7 A. Hiskia, A. Mylonas and E. Papaconstantinou, *Chem. Soc. Rev.*, 2001, **30**, 62–69.
8 Y. Chen, C. Zhang, C. Yang, J. Zhang, K. Zheng, Q. Fang and G. Li, *Nanoscale*, 2017, **9**, 15332–15339.
9 S. Kim, H. Park and W. Choi, *J. Phys. Chem. B*, 2004, **108**, 6402–6411.
10 E. Bae, J. W. Lee, B. H. Hwang, J. Yeo, J. Yoon, H. J. Cha and W. Choi, *Chemosphere*, 2008, **72**, 174–181.
11 C. Hu, Y. Zhang, L. Xu and G. Peng, *Appl. Catal., A*, 1999, **177**, 237–244.
12 J. Zhang, A. Wang, Y. Wang, H. Wang and J. Gui, *Chem. Eng. J.*, 2014, **245**, 65–70.
13 S. Damyanova, M. Cubeiro and J. Fierro, *J. Mol. Catal. A: Chem.*, 1999, **142**, 85–100.
14 K. Lv and Y. Xu, *J. Phys. Chem. B*, 2006, **110**, 6204–6212.
15 S. Ahn, S. L. Nauert, C. T. Buru, M. Rimoldi, H. Choi, N. M. Schweitzer, J. T. Hupp, O. K. Farha and J. M. Notestein, *J. Am. Chem. Soc.*, 2018, **140**, 8535–8543.
16 H.-L. Li, N. Perkas, Q.-L. Li, Y. Gofer, Y. Koltypin and A. Gedanken, *Langmuir*, 2003, **19**, 10409–10413.
17 Z. Karimi, A. Mahjoub and F. D. Aghdam, *Inorg. Chim. Acta*, 2009, **362**, 3725–3730.
18 W. Kaleta and K. Nowiska, *Chem. Commun.*, 2001, 535–536.
19 H. Hamadi, M. Kooti, M. Afshari, Z. Ghiasifar and N. Adibpour, *J. Mol. Catal. A: Chem.*, 2013, **373**, 25–29.
20 T. Kovalchuk, H. Sfihi, L. Kostenko, V. Zaitsev and J. Fraissard, *J. Colloid Interface Sci.*, 2006, **302**, 214–229.
21 W. Qi, H. Li and L. Wu, *Adv. Mater.*, 2007, **19**, 1983–1987.
22 H. Li, H. Sun, W. Qi, M. Xu and L. Wu, *Angew. Chem., Int. Ed.*, 2007, **46**, 1300–1303.
23 D. M. Fernandes, H. M. Carapuça, C. M. Brett and A. M. Cavaleiro, *Thin Solid Films*, 2010, **518**, 5881–5888.
24 D. Zhao, J. Feng, Q. Huo, N. Melosh, G. H. Fredrickson, B. F. Chmelka and G. D. Stucky, *Science*, 1998, **279**, 548–552.
25 J. S. Beck, J. C. Vartuli, W. J. Roth, M. E. Leonowicz, C. T. Kresge, K. D. Schmitt, C. T. W. Chu, D. H. Olson, E. W. Sheppard, S. B. McCullen, J. B. Higgins and J. L. Schlenker, *J. Am. Chem. Soc.*, 1992, **114**, 10834–10843.
26 Q. Huo, D. I. Margolese, U. Ciesla, P. Feng, T. E. Gier, P. Sieger, R. Leon, P. M. Petroff, F. Schüth and G. D. Stucky, *Nature*, 1994, **368**, 317.
27 T. Maschmeyer, F. Rey, G. Sankar and J. M. Thomas, *Nature*, 1995, **378**, 159.
28 C. P. Mehnert, *Chem. Commun.*, 1997, 2215–2216.
29 Y. Han, Y. Xiao, Z. Zhang, B. Liu, P. Zheng, S. He and W. Wang, *Macromolecules*, 2009, **42**, 6543–6548.
30 S. Landsmann, M. Luka and S. Polarz, *Nat. Commun.*, 2012, **3**, 1299.
31 S. Polarz, S. Landsmann and A. Klaiber, *Angew. Chem., Int. Ed.*, 2014, **53**, 946–954.
32 J. J. Giner-Casares, G. Brezesinski, H. Möhwald, S. Landsmann and S. Polarz, *J. Phys. Chem. Lett.*, 2012, **3**, 322–326.
33 J. Zhang, Y. Huang, G. Li and Y. Wei, *Coord. Chem. Rev.*, 2019, **378**, 395–414.
34 D. Y. Leung, X. Fu, C. Wang, M. Ni, M. K. Leung, X. Wang and X. Fu, *ChemSusChem*, 2010, **3**, 681–694.
35 H. Guan, L. Zhu, H. Zhou and H. Tang, *Anal. Chim. Acta*, 2008, **608**, 73–78.
36 J. Du, X. Lai, N. Yang, J. Zhai, D. Kisailus, F. Su, D. Wang and L. Jiang, *ACS Nano*, 2010, **5**, 590–596.
37 H. Zhang, X. Lv, Y. Li, Y. Wang and J. Li, *ACS Nano*, 2009, **4**, 380–386.
38 Z. Sun, L. Xu, W. Guo, B. Xu, S. Liu and F. Li, *J. Phys. Chem. C*, 2010, **114**, 5211–5216.
39 C. Chen, P. Lei, H. Ji, W. Ma, J. Zhao, H. Hidaka and N. Serpone, *Environ. Sci. Technol.*, 2004, **38**, 329–337.
40 A. Pearson, H. Jani, K. Kalantar-Zadeh, S. K. Bhargava and V. Bansal, *Langmuir*, 2011, **27**, 6661–6667.
41 Y. Guo and C. Hu, *J. Mol. Catal. A: Chem.*, 2007, **262**, 136–148.
42 N. Fu and G. Lu, *Chem. Commun.*, 2009, 3591–3593.
43 M. W. Droege, Ph.D Dissertation, University of Oregon, 1984.
44 R. G. Finke, M. W. Droege and P. J. Domaille, *Inorg. Chem.*, 1987, **26**, 3886–3896.

45 C. Comuzzi, G. Dolcetti, A. Trovarelli, F. Cavani, F. Trifirò, J. Llorca and R. G. Finke, *Catal. Lett.*, 1996, **36**, 75–79.
46 G. Baronetti, L. Briand, U. Sedran and H. Thomas, *Appl. Catal., A*, 1998, **172**, 265–272.
47 L. E. Briand, G. M. Valle and H. J. Thomas, *J. Mater. Chem.*, 2002, **12**, 299–304.
48 B. Sun, G. Zhou, C. Shao, B. Jiang, J. Pang and Y. Zhang, *Powder Technol.*, 2014, **256**, 118–125.
49 E. Papaconstantinou, *J. Chem. Soc., Chem. Commun.*, 1982, 12–13.
50 P. Seeger and R. Hjelm, *J. Appl. Crystallogr.*, 1991, **24**, 467–478.
51 O. Arnold, J.-C. Bilheux, J. Borreguero, A. Buts, S. I. Campbell, L. Chapon, M. Doucet, N. Draper, R. F. Leal and M. Gigg, *Nucl. Instrum. Methods Phys. Res., Sect. A*, 2014, **764**, 156–166.
52 G. T. Wignall and F. Bates, *J. Appl. Crystallogr.*, 1987, **20**, 28–40.
53 A. Guinier, G. Fournet and K. L. Yudowitch, *Small Angle Scattering of X-rays*, John Wiley & Sons, Inc., New York, 1955.
54 M. Kotlarchyk and S. Chen, *J. Chem. Phys.*, 1983, **79**, 2461–2469.
55 S. Berr, *J. Phys. Chem.*, 1987, **91**, 4760–4765.
56 J.-P. Hansen and J. B. Hayter, *Mol. Phys.*, 1982, **46**, 651–656.
57 K. R. Srinivasan and R. L. Kay, *J. Chem. Phys.*, 1974, **60**, 3645–3648.
58 K. V. Kumar, K. Porkodi and F. Rocha, *Catal. Commun.*, 2008, **9**, 82–84.
59 N. Fay, E. Dempsey, A. Kennedy and T. McCormac, *J. Electroanal. Chem.*, 2003, **556**, 63–74.
60 C. Kato, S. Nishihara, R. Tsunashima, Y. Tatewaki, S. Okada, X.-M. Ren, K. Inoue, D.-L. Long and L. Cronin, *Dalton Trans.*, 2013, **42**, 11363–11366.
61 M. N. Sokolov, N. V. Izarova, E. V. Peresypkina, D. A. Mainichev and V. P. Fedin, *Inorg. Chim. Acta*, 2009, **362**, 3756–3762.
62 L. Magid, K. Daus, P. Butler and R. Quincy, *J. Phys. Chem.*, 1983, **87**, 5472–5478.
63 M. Karaman, B. Ninham and R. Pashley, *J. Phys. Chem.*, 1994, **98**, 11512–11518.
64 J. Joshi, V. Aswal and P. Goyal, *J. Macromol. Sci. Phys.*, 2008, **47**, 338–347.
65 G. B. Ray, I. Chakraborty, S. Ghosh, S. Moulik and R. Palepu, *Langmuir*, 2005, **21**, 10958–10967.
66 P. Mukerjee and K. J. Mysels, *Critical micelle concentrations of aqueous surfactant systems*, National Bureau of Standard, NSRDS-NBS 36, US Goverment Printing Office, Washingtong D. C., 1971, pp. 66–67.
67 S. Vass, T. Gilanyi and S. Borbely, *J. Phys. Chem. B*, 2000, **104**, 2073–2081.
68 K. J. Mysels and R. J. Otter, *J. Colloid Sci.*, 1961, **16**, 462–473.
69 H. Gharibi and A. Rafati, *Langmuir*, 1998, **14**, 2191–2196.
70 H. Nakamura, A. Sano and K. Matsuura, *Anal. Sci.*, 1998, **14**, 379–382.
71 A. Dominguez, A. Fernandez, N. Gonzalez, E. Iglesias and L. Montenegro, *J. Chem. Educ.*, 1997, **74**, 1227–1231.
72 R. Zana, *J. Colloid Interface Sci.*, 1980, **78**, 330–337.
73 R. Zana, *Langmuir*, 1996, **12**, 1208–1211.
74 M. N. Khan, *Micellar catalysis*, CRC Press, 2006.
75 T. Wolff and B. Klaussner, *Adv. Colloid Interface Sci.*, 1995, **59**, 31–94.
76 Y. Liu, J. Goebl and Y. Yin, *Chem. Soc. Rev.*, 2013, **42**, 2610–2653.
77 C. Tanford, *J. Phys. Chem.*, 1974, **78**, 2469–2479.
78 S. G. Mitchell and M. Jesús, *J. Mater. Chem.*, 2012, **22**, 18091–18100.
79 R. Nagarajan, *Langmuir*, 2002, **18**, 31–38.
80 A. Troupis, A. Hiskia and E. Papaconstantinou, *Appl. Catal., B*, 2003, **42**, 305–315.
81 K. M. Reddy, C. G. Reddy and S. Manorama, *J. Solid State Chem.*, 2001, **158**, 180–186.
82 T. Tachikawa, S. Tojo, K. Kawai, M. Endo, M. Fujitsuka, T. Ohno, K. Nishijima, Z. Miyamoto and T. Majima, *J. Phys. Chem. B*, 2004, **108**, 19299–19306.
83 K. M. Reddy, S. V. Manorama and A. R. Reddy, *Mater. Chem. Phys.*, 2003, **78**, 239–245.
84 C. Chen, J. Li, W. Zhao, J. Zhao, L. Wan and Y. Xu, *Sci. China, Ser. B: Chem.*, 2003, **46**, 577–582.
85 C. Chen, W. Zhao, P. Lei, J. Zhao and N. Serpone, *Chem. – Eur. J.*, 2004, **10**, 1956–1965.
86 S. Yanagida, A. Nakajima, T. Sasaki, Y. Kameshima and K. Okada, *Chem. Mater.*, 2008, **20**, 3757–3764.
87 R. R. Ozer and J. L. Ferry, *Environ. Sci. Technol.*, 2001, **35**, 3242–3246.
88 A. Pearson, S. K. Bhargava and V. Bansal, *Langmuir*, 2011, **27**, 9245–9252.
89 A. Pearson, H. Zheng, K. Kalantar-zadeh, S. K. Bhargava and V. Bansal, *Langmuir*, 2012, **28**, 14470–14475.